PAPER

Check for updates

Enabling ionic transport in Li₃AlP₂: the roles of defects and disorder†

Ji Hu,[ab] Alexander G. Squires,[c] Jędrzej Kondek,[efg] Michael J. Johnson,[a] Arthur B. Youd,[d] Pooja Vadhva,[a] Partha P. Paul, [ID][hi] Philip J. Withers, [ID][i] Marco Di Michiel,[h] Dean S. Keeble, [ID][j] Michael Ryan Hansen, [ID][ef] David O. Scanlon [ID] ⋆[bc] and Alexander J. E. Rettie [ID] ⋆[ab]

Lithium phosphides are an emerging class of Li⁺ ion conductors for solid state battery applications. Despite potentially favorable characteristics as a solid electrolyte, stoichiometric crystalline Li₃AlP₂ has been reported to be an ionic insulator. Using a combined computational and experimental approach, we investigate the underlying reasons for this and show that ion transport can be induced *via* defects and structural disorder in this material. Lithium vacancies are shown to promote diffusion, and a low barrier to Li⁺ hopping of 0.2–0.3 eV is revealed by both simulations and experiment. However, polycrystalline pellets exhibit low ionic conductivity ($\approx 10^{-8}$ S cm⁻¹) at room temperature, attributed to crystalline anisotropy and the presence of resistive grain boundaries. These aspects can be overcome in nanocrystalline Li₃AlP₂, where ionic conductivity values approaching 10^{-6} S cm⁻¹ and low electronic conductivities are achieved. This approach, leveraging both defects and structural disorder, should have relevance to the discovery of new, or previously overlooked, ion conducting materials.

ᵃElectrochemical Innovation Laboratory, Department of Chemical Engineering, University College London, London, UK, WC1E 7JE. E-mail: a.rettie@ucl.ac.uk

ᵇThe Faraday Institution, Quad One, Harwell Science and Innovation Campus, Didcot, OX11 0RA, UK. E-mail: d.scanlon@bham.ac.uk

ᶜSchool of Chemistry, University of Birmingham, Edgbaston, Birmingham, B15 2TT, UK

ᵈDepartment of Chemistry, University College London, London, WC1H 0AJ, UK

ᵉInstitute of Physical Chemistry, University of Münster, Corrensstrasse 28/30, 48149 Münster, Germany

ᶠInstitute of Inorganic and Analytical Chemistry, University of Münster, Corrensstrasse 28, Münster, 48149, Germany

ᵍInternational Graduate School for Battery Chemistry, Characterization, Analysis, Recycling and Application (BACCARA), University of Münster, Münster, 48149, Germany

ʰESRF – The European Synchrotron, 71 Avenue des Martyrs, Grenoble, 3800, France

ⁱHenry Royce Institute, Department of Materials, The University of Manchester, Manchester, M139PL, UK

ʲDiamond Light Source Ltd., Diamond House, Harwell Science and Innovation Campus, Didcot, OX11 0DE, UK

† Electronic supplementary information (ESI) available. See DOI: https://doi.org/10.1039/d4ta04347b

Alex Rettie is an Associate Professor in Electrochemical Conversion and Storage in the Department of Chemical Engineering, UCL (UK). His interests are in the experimental discovery and characterisation of electrochemical energy materials and their incorporation into devices, with a focus on electronic and ionic charge transport. Prior to joining UCL, he was a post-doc at Argonne National Laboratory where he focused on materials design and total scattering techniques. He received his PhD (Chemical Engineering) from the University of Texas at Austin in 2015, investigating metal oxide photoelectrodes and his M. Eng. degree (Chemical Engineering) from the University of Edinburgh.

Alexander J. E. Rettie

This journal is © The Royal Society of Chemistry 2025

J. Mater. Chem. A, 2025, **13**, 6427–6439 | **6427**

1 Introduction

All solid-state batteries have the potential to offer high energy density and safety – crucial aspects for next generation energy storage technologies.[1] These devices require solid electrolyte (SE) materials which must have high ionic and low electronic conductivities and wide electrochemical stability windows, and be easily processible.[2] Thus, strategies to discover and optimise SEs that simultaneously meet these stringent criteria are of great interest.

High ionic conductivity ($\sigma_{ion} > 1$ mS cm^{-1}) and facile densification at room temperature have been realised in several Li-ion SE families: sulfides,[3,4] halides[5] and recently, phosphide Zintl phases.[6,7] Named after Eduard Zintl who first studied them,[8,9] these are solid-state compounds formed between metals from groups 1 and 2 and elements from groups 13 and 14. Such materials exhibit characteristics that should produce good SE candidates, namely: a tendency towards open framework structures (beneficial for ion transport), as well as being poor electronic conductors (semiconducting).[10] Additionally, the phosphide anion is relatively large and polarisable; aspects thought to be favourable for facile ion migration and room temperature deformability.[11,12]

The reported ternary Li–M–P phases (M = Al, Si, Ga, Sn)[6,7,13,14] by Fässler and co-workers support this rationale. The most lithium-rich member in the Li–Al–P phase space, Li$_9$AlP$_4$ achieved $\sigma_{ion} \approx 3$ mS cm^{-1} at room temperature, with a computational study confirming low barriers to ion migration in Li–M–P compounds.[15] Despite its similarity to Li$_9$AlP$_4$ in AlP$_4$ structural motifs, 50 at% Li content and 3D ion migration pathways (Fig. 1), stoichiometric Li$_3$AlP$_2$ was recently reported to be an ionic insulator by impedance spectroscopy.[16]

Strategies to introduce vacancies or excess mobile ions are commonly employed to increase the σ_{ion} of SE materials.[17,18] Additionally, the disordered or nanocrystalline materials produced via high energy ball milling have recently expanded the toolbox to realise new SEs. This has been demonstrated in the ternary lithium halides: mechanosynthesised Li$_3$YCl$_6$ exhibited diffraction patterns with broad peaks – consistent with nanocrystallinity – and high σ_{ion} values,[5] and in the case of Li$_3$ErI$_6$,

where the as-milled phase had a higher σ_{ion} compared to the material after thermal annealing.[19] Similar phenomena has been reported for some sulfide electrolytes, namely Li$_6$PS$_5$I and Li$_4$PS$_4$I, where nanocrystalline materials outperformed their microcrystalline counterparts.[20,21] Although whether this kind of disorder is positively or negatively correlated with σ_{ion} is highly material-specific,[22] the utility of ball milling to access non-equilibrium ion conducting phases is clear. To the best of our knowledge, the effects of non-stoichiometry or structural disorder on ionic conduction in ternary phosphides have not been reported so far.

Here, we investigate defect engineering approaches as a means of improving the solid electrolyte properties of Li$_3$AlP$_2$. First, calculations are performed to evaluate the defect chemistry and Li ion transport in this material. Vacancy assisted Li-ion hopping is shown to be the most favourable mechanism with a low activation energy, but a low native defect concentration and anisotropy appear to limit ionic transport. We then synthesise non-stoichiometric nanocrystalline and crystalline powders via mechanical ball milling and thermal treatments. Although a low microscopic hopping barrier is confirmed experimentally in crystalline Li$_3$AlP$_2$, a poor macroscopic conductivity is measured on pellets by impedance spectroscopy. Nanocrystalline Li$_3$AlP$_2$ materials are shown to exhibit at least one order of magnitude higher ionic conductivity than their crystalline counterparts while maintaining low electronic conductivity. This result is attributed to both a disruption of slow inter-layer ion transport and reduced grain boundary resistance. These results further our understanding of materials design strategies for SEs and suggest structurally disordered analogues of crystalline materials are worthy of (re-)investigation via combined theoretical and experimental approaches. Although our focus here is SEs, ternary,[23] and higher,[24] metal phosphides have also shown promise as high-capacity electrode materials that could benefit from such strategies to improve ion transport.

2 Methodology

2.1 Computational methods

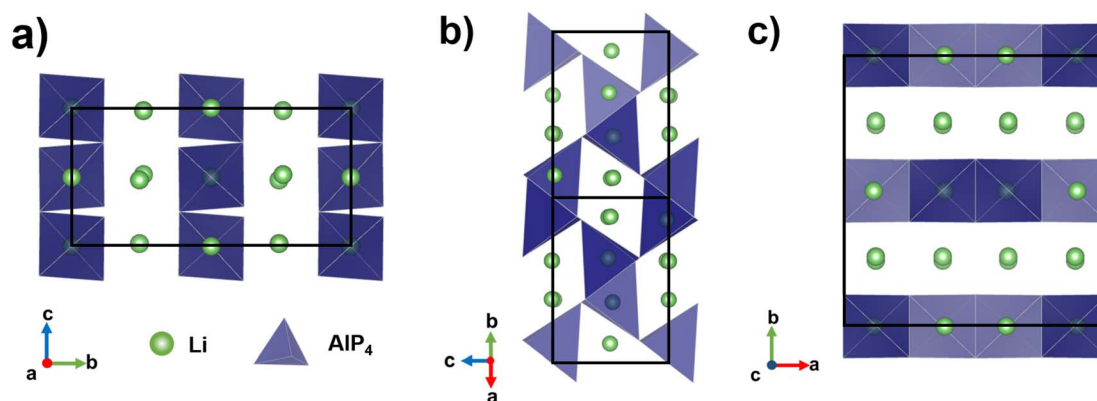DFT calculations were carried out using the Vienna *Ab initio* Simulation Package (VASP) with Projector Augmented Wave

Fig. 1 Crystal structure of orthorhombic Li$_3$AlP$_2$,[16] the unit cell is shown in solid black lines. AlP$_4$ tetrahedra are shown in blue and Li atoms in green. Li$^+$ layers in the *a* and *c* axes are notable in (a) and (c). Intralayer Li$^+$ channels are highlighted in (b).

6428 | *J. Mater. Chem. A*, 2025, **13**, 6427–6439

This journal is © The Royal Society of Chemistry 2025

(PAW) pseudopotentials.[25–28] Nudged elastic band (NEB) and *ab initio* molecular dynamics (AIMD) simulations were performed using the GGA functional PBEsol.[29] Band structures, density of states, and defect formation energies were calculated using the hybrid functional HSE06.[30,31] A 450 eV energy cutoff for the plane wave basis set was used, and was increased by 30% for calculations which allowed for the cell volume to change. A Γ-centered Monkhorst–Pack k-point grid with a density of 0.27 Å^{-1} was used to sample reciprocal space. Defect, AIMD and NEB calculations were all carried out in supercells with cell lengths greater than 10 Å to minimise interactions between periodic-images (full methodological details for the defect calculations can be found in the ESI†). Self-consistent field cycles were deemed converged when energy differences between successive cycles fell within 1×10^{-6} eV and structural relaxations were deemed converged when forces on all atoms fell below 0.005 eV per atom (this tolerance was increased to 0.01 eV per atom for the NEB calculations). For each AIMD simulation, two equilibration stages were performed, first using a 2 ps NVE run with temperature rescaling every 50 steps, followed by a 2 ps NVT run. The production NVT simulations were run for 95 ps.

Mean squared displacements from the AIMD trajectories were calculated using the KINISI software package.[32,33] CPLAP was used for calculating chemical potential limits.[34] Self-consistent Fermi energies, transition level diagrams and defect concentrations were calculated using the py-sc-fermi software package.[35] Ancillary analysis used the doped,[36,37] scipy,[38] numpy,[39] pandas,[40] ASE,[41] pymatgen,[42] sumo[43] and phonopy[44,45] python libraries.

2.2 Synthesis

All chemical handling was performed in an Ar-filled glovebox (MBraun, <1 ppm H_2O and O_2), because of flammable/air-sensitive precursors, intermediate and final products. To produce Li_3AlP_2 powders, stoichiometric amounts of lithium metal wire (3.2 mm dia., Alfa Aesar, 99.8%), aluminium powder (Alfa Aesar, 325 mesh, 99.5%) and red phosphorous powder (Sigma-Aldrich, ≥97.0) were mixed in a mortar and pestle before ball milling in a tungsten carbide (WC) milling jar containing three WC balls, dia. 15 mm each. A planetary ball mill (Retsch PM 100) was used to mill the materials at 350 rpm (10 min on and 3 min off) for 36 hours total. Before annealing, crucibles and ampules were dried in a drying oven overnight and transferred to a glovebox for assembly. The milled powders were loaded into an alumina crucible (Almath) and carefully placed in fused silica (Multi-lab) ampule followed by an alumina cap. The fused silica ampule was then evacuated and flame-sealed under 3–6 mTorr. These assemblies were annealed upright at three different temperatures: 300, 500, and 700 °C for 12 h in a box furnace (Carbolite-Gero CWF 1200).

2.3 X-ray diffraction

Lab-based X-ray diffraction (LXRD) and synchrotron X-ray diffraction (SXRD) were carried out to check the phase purity and obtain crystallographic information. LXRD was conducted using a Rigaku Smartlab SE diffractometer with a Mo X-ray

source (wavelength = 0.71 Å). The 2θ angle scanning range was from 5° to 40° with a scan speed of 0.8° min^{-1}. Air-sensitive Li_3AlP_2 powder was protected from air and moisture by sealing Kapton tape against the top of the sample holder in an Ar-filled glovebox. SXRD experiments were performed at the European Synchrotron Radiation Facility (ESRF; ID15A,[46] wavelength = 0.2479 Å) for as-milled and 300 °C annealed samples, and at Diamond Light Source (I15, wavelength = 0.1722 Å) for 500 °C annealed samples. All powder samples were flame-sealed under 3–6 mTorr in borosilicate glass capillary tubes (Capillary Tube Supplies Ltd., outer dia. 1.5 mm). The crystal structure and simulated diffraction patterns were analysed using VESTA software.[47] Rietveld refinement was conducted using TOPAS software (version 7.21).

2.4 Pair distribution function (PDF) analysis

X-ray scattering measurements were performed at the ESRF (beamline ID15A) using powder samples flame-sealed in fused silica capillaries (identical sample preparation to the SXRD experiments detailed in Section 2.3). The wavelength of X-rays were 0.2479 Å and 0.1239 Å for the 300 °C and 500 °C annealed samples respectively. pyFAI[48] software was used for integration and background subtraction. The transformation from $S(Q)$ to $G(r)$ was done using PDFgetX3 (ref. 49) software, with maximum momentum transfer vector $Q_{max} = 15$ Å^{-1} and small box modelling of the local structure performed with PDFgui software.[50]

2.5 Nuclear magnetic resonance spectroscopy

Single-pulse ^6Li, ^{27}Al and ^{31}P magic-angle spinning (MAS) NMR experiments to investigate the local structure were performed on a Bruker DSX 500 spectrometer equipped with a wide-bore superconducting magnet operating at 500.39 MHz (11.75 T) using a VTN broadband probe and zirconia rotors with outer dia. 4 mm packed under Ar atmosphere. Larmor frequencies of the studied nuclei were 73.6 MHz (^6Li), 130.3 MHz (^{27}Al), 202.5 MHz (^{31}P). A MAS frequency of 10.00 kHz was used for all nuclei. MAS NMR experiments for all samples were performed using the following pulse lengths, flip angles: 5.50 μs, 90° (^6Li), 2.00 μs, 90° (^{27}Al), 4.00 μs, 45° (^{31}P). To ensure quantitative spectra the following relaxation delays were used: 180 s (^6Li), 2 s (^{27}Al), 30 s (^{31}P). The obtained MAS NMR spectra were referenced to ^6Li-enriched Li_2CO_3 (0.1 ppm), 1 M Al(NO$_3$)$_3$ (0 ppm) and 1 M H$_3$PO$_4$ (0 ppm) for ^6Li, ^{27}Al, and ^{31}P respectively.

Single-pulse static ^7Li NMR experiments with varying temperature were performed on a Bruker Advance III 300 spectrometer equipped with a wide-bore magnet which operates at 300.15 MHz (7.05 T) using a VTN broadband probe and zirconia rotors with outer dia. 4 mm packed under Ar atmosphere. All experiments were conducted at a resonance frequency of 116.6 MHz (^7Li) with a pulse length of 2.50 μs for a 90° pulse, corresponding to a nutation frequency of 100 kHz. The temperature of the sample was regulated by using a nitrogen gas flow and electrical heating. In the temperature range between 165–210 K, a heated nitrogen dewar tank was used; between 200–300 K, an Air Jet XR compressor-based

This journal is © The Royal Society of Chemistry 2025

J. Mater. Chem. A, 2025, **13**, 6427–6439 | **6429**

cooling system from SP Scientific (FTS Systems); between 300–420 K, an uncooled nitrogen gas flow was used. ^{1}H NMR spectra of methanol (176–290 K) and ethylene glycol (320–440 K) were recorded to calibrate the temperature with the occurring shifts in signal frequency. Extrapolation of the indicated temperature *versus* recorded chemical shift function was used to calibrate temperature points below the freezing point of methanol.

The full width at half maximum (FWHM) were extracted from the varying temperature static ^{7}Li NMR spectra in order to obtain activation energies (E_a) for Li$^+$ ion transport, using the Hendrickson–Bray equation given by:

$$\Delta\nu(T) = \frac{\Delta\nu_R}{1 + \left(\frac{\Delta\nu_R}{\Delta\nu_E} - 1\right)\exp\left(-\frac{E_a}{k_B T}\right)} + \Delta\nu_C \quad (1)$$

where, k_B is the Boltzmann constant, T is the temperature, $\Delta\nu_C$ is the temperature independent line broadening. The low temperature plateau can be described by $\Delta\nu(T \to 0 = \Delta\nu_R + \Delta\nu_C)$, a high temperature plateau can be described by $\Delta\nu(T \to \infty = \Delta\nu_E + \Delta\nu_C)$ and E_a is the activation energy.

2.6 Cell fabrication

Solid-state electrochemical characterisation was performed using a cylindrical cell where pressure could be applied, based on the design reported by Randau *et al.*[51] In a typical experiment, 0.15 g of powder was added to the PEEK cell chamber (8 mm dia.) and uniaxially pressed (pressure = 130 MPa, measured using a load cell) to form a pellet between two stainless steel plungers that functioned as ion-blocking electrodes. This process resulted in an approximate pellet density of 1.5 g cm^{-3} (>80% of theoretical). To assemble the Li|SE|Li cell configuration, lithium metal discs (Goodfellow, 0.1 mm thickness) were punched to 7 mm in diameter and placed either side of the pellet.

2.7 Electrochemical and electronic characterisation

A potentiostat (ref. 600+, Gamry) was used for electrochemical and electronic measurements in the cells described previously at room temperature in an Ar-filled glovebox. Electrochemical impedance spectroscopy (EIS) was conducted using a 10–50 mV perturbation voltage range over a frequency range of 0.1–1 MHz. The EIS data were fit using an equivalent circuit model (ECM) assisted by Kramers–Kroenig analysis as well as the distribution of relaxation times (DRT) method[52] using DRTtools software.[53] Based on the bulk resistance (R) obtained through EIS measurements, the σ_{tot} was calculated through eqn (2),

$$\sigma_{tot} = \frac{l}{RA} \quad (2)$$

where, l is the thickness and A is cross-section area of the pellet. DC polarisation experiments were used to estimate the electronic conductivity (σ_e) of cold-pressed pellets. A constant voltage of 0.5 V was applied for 2 to 5 h and the resulting current–voltage curve fit to an exponential decay function to extract the electronic leakage current. The electronic resistance was calculated from the voltage (0.5 V) and final electronic

leakage current. The ionic conductivity (σ_{ion}) was then determined using eqn (3):

$$\sigma_{tot} = \sigma_{ion} + \sigma_e \quad (3)$$

where, σ_{ion} contains impedances due to the bulk and grain boundaries if present.

3 Results and discussion

3.1 Computational investigation of crystalline Li$_3$AlP$_2$

First reported by Juza and Schulz in 1952,[54] Li$_3$AlP$_2$ consists of alternating corner and edge-sharing AlP$_4$ tetrahedra that form a layered structure perpendicular to the *b* axis with pure Li layers separated by mixed Li/Al slabs (Fig. 1). The 3D connectivity of the Li$^+$-containing channels and layers suggest facile ion diffusion may be possible in this structure. The crystal structure has been indexed as orthorhombic, both as *Ibca* (no. 73)[54] and *Cmce* (no. 64),[16] – this study assumes the symmetry of *Cmce* (no. 64) to be consistent with the latest literature. Table 1 shows a comparison between the lattice parameters predicted by the two functionals as compared to experiment. Generally, PBEsol slightly overestimated the lattice parameters while HSE06 underestimated them, but all values are within 1% of the experimental lattice parameters.

Our electronic structure calculations (Section S1 in the ESI†) confirmed previous results for this compound,[16,55] *i.e.*, a direct band gap with magnitude in agreement with the experimentally measured absorption onset of ≈ 2.4 eV.[56] However, phonon, defect and molecular dynamics calculations had not been performed for Li$_3$AlP$_2$. Phonon calculations indicated a stable phase with the phonon band structure shown in Fig. S1.2 in the ESI.†

To understand potential diffusion mechanisms in orthorhombic Li$_3$AlP$_2$, we performed two AIMD simulations, a system containing a lithium vacancy and a system containing a lithium interstitial. The lithium mean squared displacements (MSD) for the two systems simulated for 95 ps at 900 K are shown in Fig. 2. The MSD for the vacancy system rises more quickly with time, suggesting faster diffusion in the lithium deficient system than the lithium-rich system and vacancy diffusion as the dominant transport mechanism in Li$_3$AlP$_2$. To obtain more insight into the diffusion processes in the vacancy containing cell, we assigned lithium site occupancies over the simulation timescale and tracked which sites the hops occur between. We can assign these hops as either intra- or inter-layer, and more specifically as between the Li-layer and the mixed Li/Al layer, or within

Table 1 Comparison between Li$_3$AlP$_2$ lattice parameters predicted by the two functionals as compared to experiment

	PBEsol (Å)	HSE06 (Å)	Experiment (Å)
a	11.56	11.44	11.51
b	11.80	11.66	11.76
c	5.84	5.77	5.82

6430 | *J. Mater. Chem. A*, 2025, **13**, 6427–6439

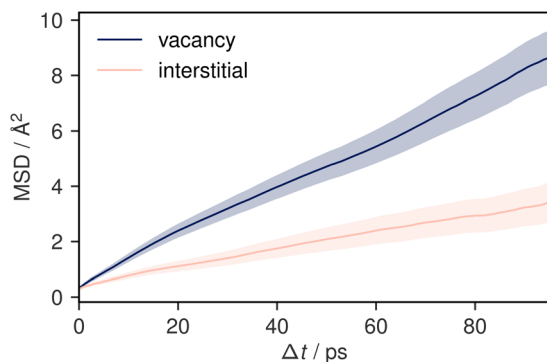This journal is © The Royal Society of Chemistry 2025

Fig. 2 Mean squared displacement plots for two 95 ps simulations of Li_3AlP_2 simulated at 900 K. One simulation cell contains a vacancy and the other, an interstitial. The shaded areas show a 95% confidence interval in the mean-squared displacement.
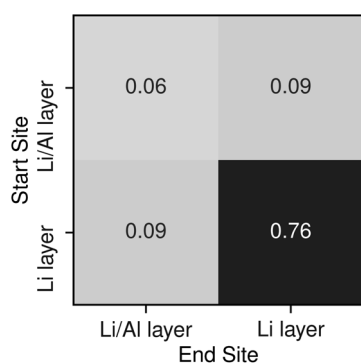

Fig. 3 Transition frequencies between the different lithium sites in a Li_3AlP_2 supercell containing a single vacancy taken from a 95 ps AIMD simulation at 900 K.

them. This yields three types of hop: between the sites in the mixed layer, between the sites in the lithium layer, or hopping from one layer to the other. The frequency of each of these hops over the simulation timescale is plotted in Fig. 3. It is immediately clear from these simulations that the transport in Li_3AlP_2 is anisotropic, with the vast majority of hops occurring

within the Li-layer, only relatively rarely did lithium hop between layers.

To further confirm and characterise the anisotropic lithium transport in Li_3AlP_2, we calculated climbing-image nudged elastic band (NEB) simulations on each symmetry-independent vacancy hop in crystalline Li_3AlP_2. The calculated energy profile for these hops are shown in Fig. 4. In general, the barriers were highest for the hops between layers and lower for hops within them, in line with the observed anisotropy in the AIMD simulations. The intralayer hopping within the mixed Li/Al layer had the lowest barrier, however, the higher energy of the end points relative to those within the lithium layer explained why this hop is less frequent in the AIMD simulation: even though the barrier was lower for hopping in the Li/Al layer, lithium vacancy formation in the mixed layer was less energetically favourable, and so these sites were less likely to be depopulated, reducing the occurrence of this hopping process. For comparison, the direct interstitial hopping barrier was greater that 1 eV, and an interstitialcy mechanism returned a barrier of 0.58 eV (Fig. S1.3 in the ESI†).

The assumption of vacancy-mediated transport in Li_3AlP_2 is predicated on lithium vacancies being a major defect species in Li_3AlP_2. To confirm this, we characterised the defect chemistry in Li_3AlP_2 as a function of elemental chemical potentials.[57] Under all conditions, the highest concentration point-defects were lithium interstitials and vacancies approximately corresponding to Frenkel-defect dominated defect chemistry. All defects with concentrations above 1×10^8 cm^{-3} under lithium-poor conditions are shown in Fig. 5. This result again supports the possibility of vacancy dominated transport. However, it is worth noting that these defect concentrations correspond to less than 0.01% of lithium sites being vacant and of the interstitial sites being occupied, *i.e.*, despite the reasonably low barriers for vacancy hopping, Li_3AlP_2 is fully ordered and, under a thermodynamic regime, has low defect concentrations.

Taken together, this computational analysis pointed to two potential limiting factors for facile long-range conductivity in Li_3AlP_2: diffusion and defect formation anisotropy results in effective 2D transport in a system which on visual inspection may be assumed to have 3D transport. This may increase grain
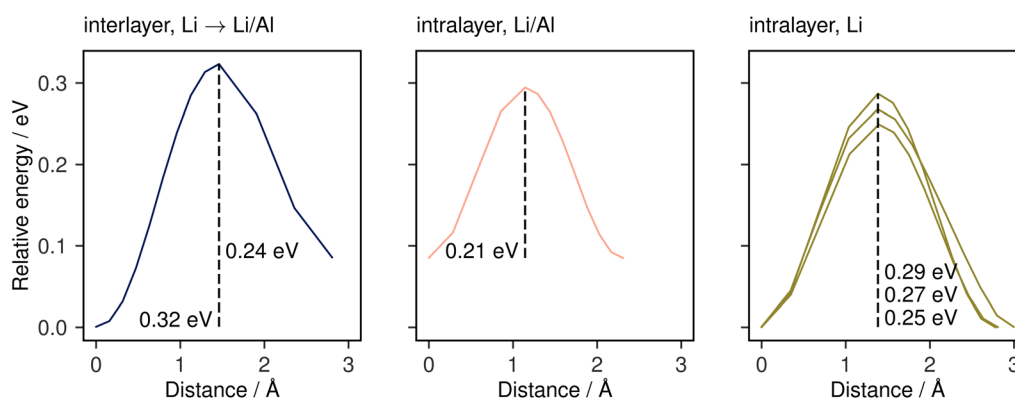

Fig. 4 Climbing-image NEB barriers calculated for each symmetrically distinct near-neighbour vacancy-mediated Li-diffusion pathway in Li_3AlP_2 categorised by the identity of the end-member lithium sites. These pathways are shown schematically in the ESI, Fig. S1.3.†

This journal is © The Royal Society of Chemistry 2025

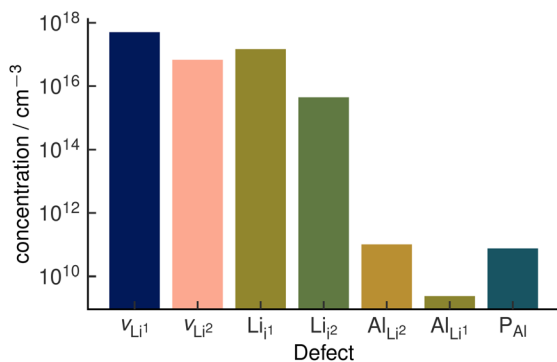J. Mater. Chem. A, 2025, 13, 6427–6439 | **6431**

Fig. 5 Defect concentrations in orthorhombic Li_3AlP_2 calculated under thermodynamic equilibrium. The two unique Li sites are discretised with the notation site Li^1 and site Li^2. Site Li^1 refers to the lithium site in the Li layer. Site Li^2 refers to the lithium site in the mixed Li/Al layer. The positions of the two interstitial sites are shown in the ESI, Fig. S1.†

boundary resistance by introducing strong grain-orientation dependence on transport and in addition, low defect concentrations in an ordered system results in an effective low carrier concentration, further limiting conductivity. Therefore, strategies to improve ionic conductivity in Li_3AlP_2 should aim to overcome these limitations, disrupting the anisotropic diffusion pathways and increasing the charge carrier concentrations.

3.2 Experimental investigation of Li_3AlP_2

3.2.1 Synthesis and structural characterisation. First, LXRD was used to investigate the influence of annealing temperature on nominally stoichiometric Li_3AlP_2 powders (Fig. 6a). Interestingly, the powder products after milling without heat treatment showed broad peaks consistent with Li_3AlP_2, indicating some degree of reaction by mechanochemical synthesis alone. These features increased in intensity and narrowed after annealing at 300 °C and 500 °C, before impurity peaks for LiP and Li_3P emerged after 700 °C treatment. To target defective materials with lithium vacancies and/or interstitials, samples with various Li contents ($x = -2.5$, 0 and 2.5% in $Li_{3(1+x)}AlP_2$) were prepared. However, due to the limited resolution of LXRD, as well as large background signal from the Kapton tape used to protect the air sensitive samples, synchrotron XRD was conducted to better analyse sample purity and crystal structure.

Using SXRD, the as-milled material was shown to exhibit multiple secondary phases and a broad background that were not observable by LXRD (Fig. S2.1 in the ESI†). Due to the phase inhomogeneity of this sample, it was not analysed further. In contrast, Li_3AlP_2 was obtained as the majority phase in both 300 °C and 500 °C treated samples (Fig. 6b and c).

No crystalline secondary phase was observed for 300 °C-treated $Li_{3(1+x)}AlP_2$ powders (Fig. 6c), but the peaks were noticeably broad, suggesting nanocrystallinity, *i.e.*, nanocrystalline domains in an amorphous matrix. Rietveld refinement using the Scherrer equation[58] was performed, resulting in an estimated crystallite size of ≈ 23 nm. In addition to the orthorhombic Li_3AlP_2 phase, a Li_9AlP_4 minor phase was

detected for samples annealed at 500 °C, whose intensity decreased with decreasing x (Fig. 6b). Rietveld refinement (Fig. 6d) was carried out for the most phase-pure sample: $Li_{2.925}AlP_2$, resulting in a Li_9AlP_4 phase fraction of ≈ 3.5 wt%. Application of the Scherrer equation in this case resulted in a domain size > 170 nm, indicating micron-scale crystallites as expected[59] (all crystallographic and refinement parameters can be found in Section S2 in the ESI†).

Based on the above analyses, the samples annealed at 500 °C and 300 °C will be identified as microcrystalline (μc-$Li_{3(1+x)}AlP_2$) and nanocrystalline (nc-$Li_{3(1+x)}AlP_2$) respectively for the remainder of the manuscript. The disordered nature of nc-$Li_{3(1+x)}AlP_2$ motivated us to probe the local structure and the presence of any non-crystalline phases in these samples by pair-distribution-function (PDF) analysis and solid state NMR spectroscopy.

PDF analyses (Fig. 6e and f) revealed similar local structures for nc- and μc-$Li_{3(1+x)}AlP_2$ that could both be well-represented by the long range orthorhombic crystal structure. Full refinement details can be located in Section S7 in the ESI.† In nanocrystals and nanocrystalline materials, the coherence length can be estimated by modelling the PDF intensity with increasing r, as atomic correlations dissipate beyond the spatial extent of the crystalline nanodomains.[60,61] Attempts to extract this quantity resulted in a lower limit of ≈ 20 nm for domains in nc-$Li_{3(1+x)}$-AlP_2, consistent with the results of Rietveld refinement.

The obtained MAS NMR spectra are presented in Fig. 7 for ^6Li, ^{27}Al and ^{31}P. Orange vertical lines at marked chemical shifts were added to the ^6Li, ^{27}Al and ^{31}P spectra to indicate the resonances corresponding to the crystalline Li_3AlP_2 phase,[16] as well as green vertical lines to mark sample impurities and their relative shift. Spinning sidebands are marked with asterisks in all spectra. For clarity, the most phase-pure $Li_{3(1+x)}AlP_2$ samples ($x = -2.5\%$) are presented in the main text, with data for all samples contained in the ESI (Fig. S3.1†).

As can be seen in Fig. 7, three distinct Li signals are present in all ^6Li MAS NMR spectra. Two of these, with ^6Li chemical shifts of 4.0 and 3.0 ppm, are attributed to the two nonequivalent crystallographic positions for Li in the Li_3AlP_2 crystal structure. However, depending on the annealing temperature and as a result thereof the level of crystallinity, the two Li signals become better resolved in the micro-crystalline compared to the nanocrystalline sample (Fig. 7a). A third ^6Li signal at 0.7 ppm is also present, resulting from an unknown impurity. The intensity of this peak is much higher for the nc-$Li_{2.925}AlP_2$ sample (Fig. 7b). It can be also noted that the ^6Li signal at 0.7 ppm is much less intense in the μc-$Li_{2.925}AlP_2$ compared to other microcrystalline compositions (Fig. S3 in ESI†). This is in agreement with SXRD refinement results (Fig. 6d) and suggests the lithium deficient sample has the least amount of impurities among all μc-$Li_{3(1+x)}AlP_2$ powders.

In the ^{27}Al MAS NMR spectra presented in Fig. 7, the ^{27}Al signal at 137 ppm may be assigned to the single nonequivalent Al position of the crystal structure for Li_3AlP_2.[16] The ^{27}Al chemical shift is in agreement with aluminum in a tetrahedrally coordinated position as previously reported,[62] whereas the ^{27}Al signal linewidths reflect the sample crystallinity, *i.e.*, the
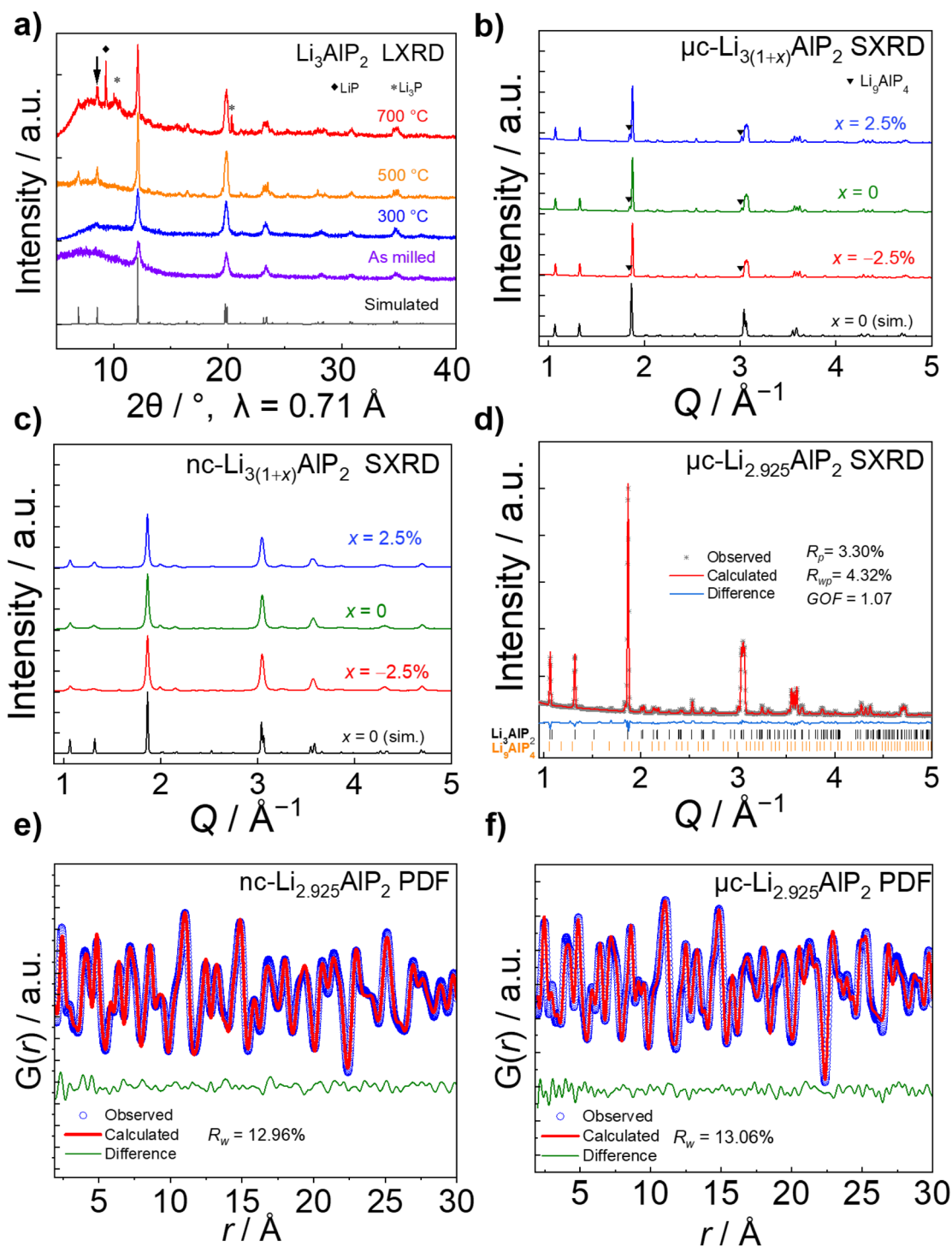
6432 | *J. Mater. Chem. A*, 2025, **13**, 6427–6439

This journal is © The Royal Society of Chemistry 2025

Fig. 6 Structural characterisation of $Li_{3(1+x)}AlP_2$ (a) Lab XRD of Li_3AlP_2 products after different annealing temperatures. (b) Synchrotron XRD of 500 °C annealed, micro-crystalline μc-$Li_{3(1+x)}AlP_2$, and (c) 300 °C annealed, nano-crystalline nc-$Li_{3(1+x)}AlP_2$. (d) Rietveld refinement for μc-$Li_{2.925}AlP_2$. Pair distribution function analyses of (e) nc-$Li_{2.925}AlP$ and (f) μc-$Li_{2.925}AlP_2$.

linewidth decreases with annealing temperature. In addition, ^{27}Al signals at 80 ppm for the samples in Fig. 7 can be observed. These signals can be attributed to sample impurities and were observed in all samples at similar chemical shifts (Fig. S3 in ESI†). Similar to the ^6Li data, μc-$Li_{2.925}AlP_2$ has the weakest impurity peaks compared to all other samples.

In the ^{31}P MAS NMR spectra presented in Fig. 7, two ^{31}P resonances at −300 and −310 ppm can directly be assigned to the two crystallographic nonequivalent phosphorous positions in the Li_3AlP_2 crystal lattice. Once again a clear narrowing and splitting of signals can be observed due to increased crystallinity. This can be even better seen in the ^{31}P MAS NMR spectra
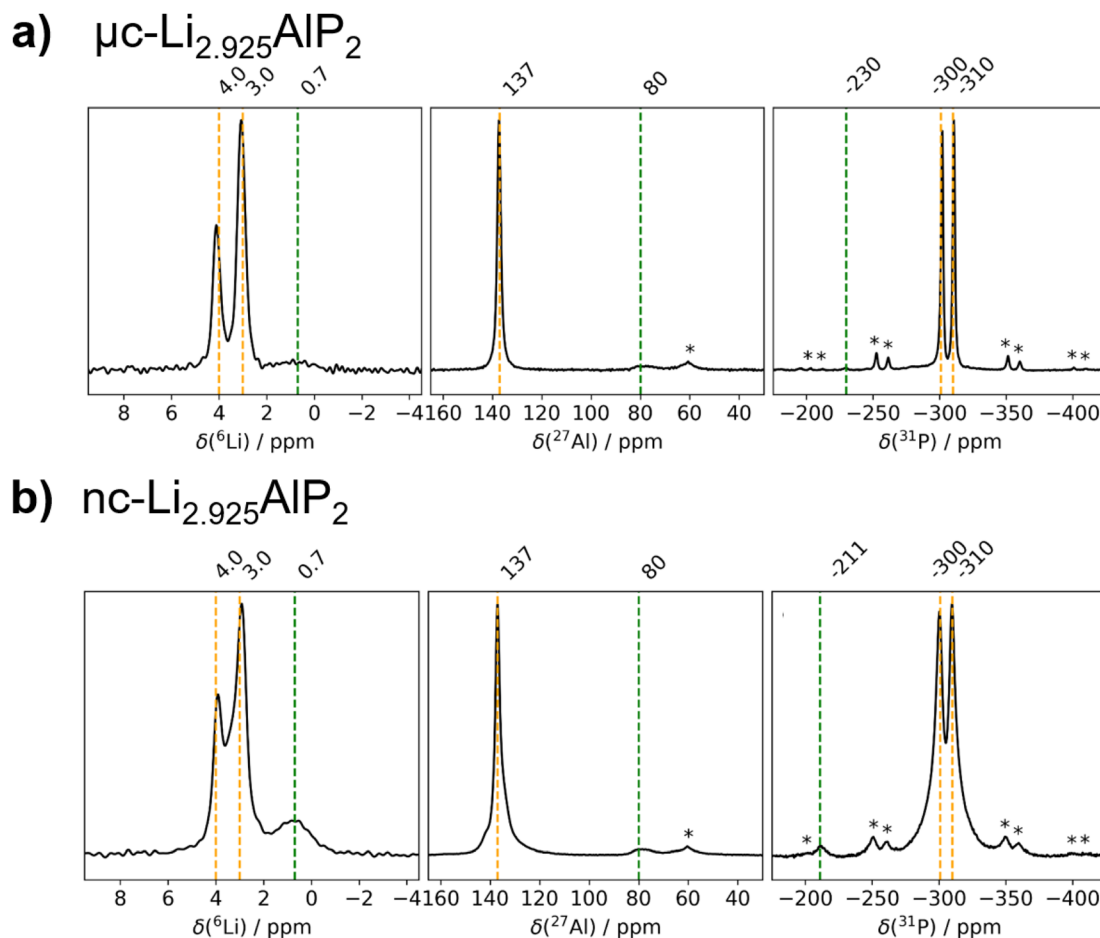
This journal is © The Royal Society of Chemistry 2025

J. Mater. Chem. A, 2025, **13**, 6427–6439 | **6433**

Fig. 7 ^6Li, ^{27}Al and ^{31}P MAS NMR spectra of $Li_{3(1+x)}AlP_2$. (a) μc-$Li_{2.925}AlP_2$ and (b) nc-$Li_{2.925}AlP_2$ recorded with a MAS frequency of 10.0 kHz (11.75 T).

presented in (Section S3 in ESI†) for stoichiometric samples. Different impurity peaks can be identified for both the samples presented in Fig. 7, as well as those in (Fig S3.1 in ESI†). Once again it can be noted that the μc-$Li_{2.925}AlP_2$ sample shows only one impurity peak at −230 ppm with very low intensity.

From the fact that all probed nuclei show impurities it can be speculated that there is a secondary Li–Al–P phase with a different stoichiometry compared to Li_3AlP_2. This is in agreement with SXRD detecting Li_9AlP_4 minor phase, although assignment of the impurity peaks to a specific phase was not possible from the MAS NMR spectra. It is likely these are minor amorphous Li–Al–P phases and could describe the amorphous matrix expected in the case of nanocrystalline materials.

3.2.2 NMR ion dynamics. Li^+ ion dynamics in the studied samples were followed *via* static ^7Li lineshape analysis in the temperature range from 167 K to 415 K. Normalised spectra centered at 0 Hz are presented for both μc-$Li_{2.925}AlP_2$ (Fig. 8a) and nc-$Li_{2.925}AlP_2$ (Fig. 8c). Similar spectra for the other samples are presented in (Fig. S4.1 in ESI†). From the ^7Li NMR spectra two components to the total signal were identified (one broad and one narrow). Previous literature reported for the lithium aluminum sulfides, Li_3AlS_3 and $Li_{4.3}AlS_{3.3}Cl_{0.7}$ suggest that these two components might be attributed to slow Li^+ migration

for the broad signal and fast Li^+ migration for the narrow signal.[63] Based on our simulations, it might be assumed that in case of Li_3AlP_2, the fast transport would correspond to the intralayer migration of Li^+ ions, while the slow component corresponds to the interlayer migration of Li^+ ions. Spectral deconvolution of the two ^7Li signal was challenging, as signals are centered in the same position. Because of this, fitting became unreliable at lower temperatures, where two partial ^7Li signals coalesced. For this reason, the data are regarded as a global movement of Li^+ ions within the sample instead of two distinct migration pathways for further analysis.

The FWHM are plotted against temperature in Fig. 8 for all microcrystalline (b) and nanocrystalline (d) samples. Data were fit using eqn (1) (marked with dashed lines in plots) in order to calculate activation energies (E_a) for Li^+ ion transport. Obtained activation energies for microcrystalline, nanocrystalline and the as-milled samples can be located in Table S4.1 in the ESI.† E_a values for all samples are within their margin of error (0.2–0.3 eV), regardless of composition and annealing treatment. These NMR data are in strong agreement with the calculated NEB barriers. This indicates that the dominant microscopic Li^+ ionic transport mechanism is the same in all samples and pertains to the majority phase: Li_3AlP_2.
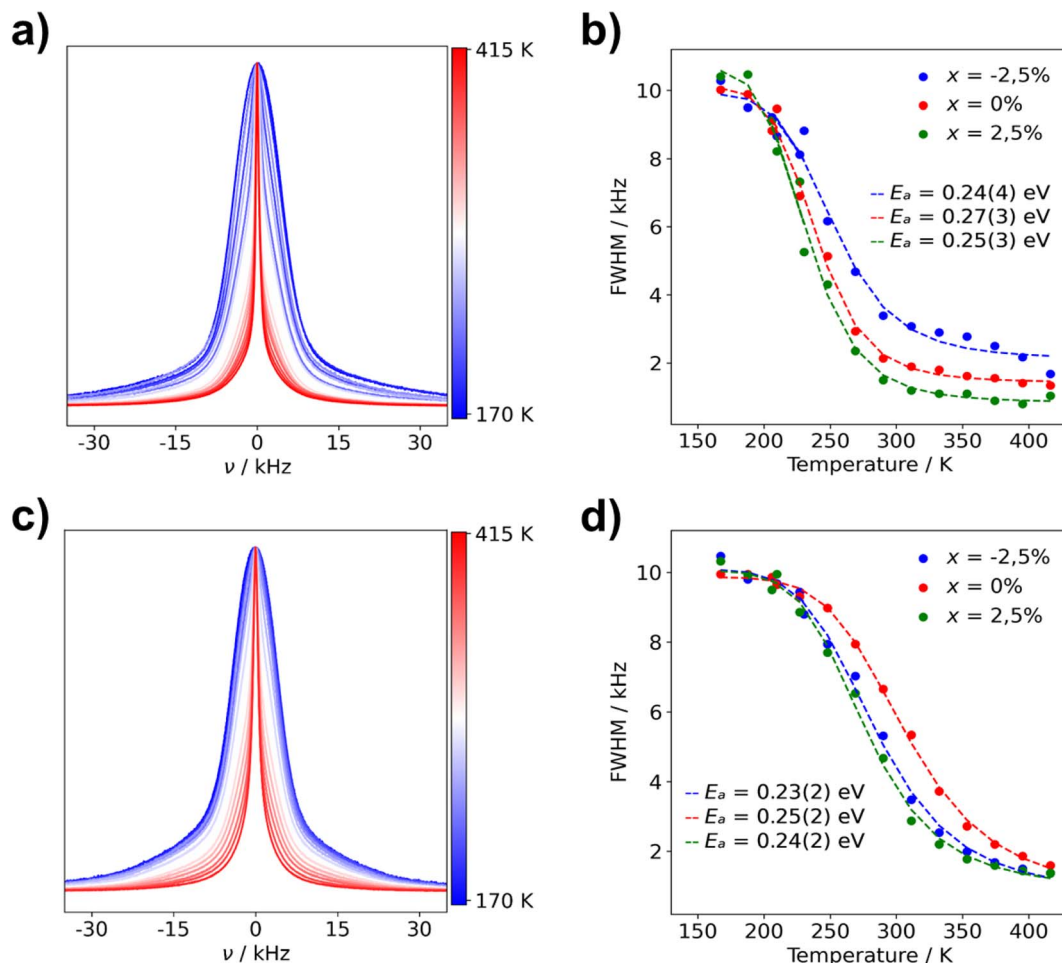
6434 | *J. Mater. Chem. A*, 2025, **13**, 6427–6439

This journal is © The Royal Society of Chemistry 2025

Fig. 8 Normalized static ^{7}Li NMR spectra and FWHM of Li$_{3(1+x)}$AlP$_2$ for (a) µc-Li$_{2.925}$AlP$_2$ ^{7}Li NMR spectra (b) µc-Li$_{3(1+x)}$AlP$_2$ FWHM fit with eqn (1) and (c) nc-Li$_{2.925}$AlP$_2$ (d) nc-Li$_{3(1+x)}$AlP$_2$ FWHM fit with eqn (1). The used color gradient ranges from blue (low temperatures) to red (high temperatures) to indicate the change of lineshapes with temperature.

3.2.3 Electrochemical and electronic measurements.

To probe the bulk electrochemical response of Li$_3$AlP$_2$, EIS was performed on cold-pressed pellets contacted using stainless steel blocking electrodes. EIS in a symmetrical Li|SE|Li config-uration yielded equivalent results (Fig. S5.1 in the ESI†). µc-Li$_3$AlP$_2$ samples showed large impedance values for all compositions – these data were fit using an equivalent circuit model (ECM) with three R-CPE units in series (Fig. 9a), consis-tent with polarisation features observed in the ranges 10^{-5} to 10^{-4}, 10^{-4} to 10^{-3} and $\approx 10^{-2}$ s by DRT analysis (Fig. S5.2 in the ESI†). Although a case could made to add a fourth polarisation feature from the DRT, we chose to use the minimum number of elements needed to represent the data and preserve physical meaning. Extracted capacitance values for the two faster processes were in the low 10^{-11} F range (Table S5.1 in the ESI†), suggestive of bulk and grain boundary conduction.[64] Therefore, the fastest processes are assigned to bulk conduction, the moderate timescale features to grain boundaries, with the final, slowest process being an interfacial charge transfer impedance. In all cases, the grain boundary feature was the largest contributor to the total impedance. Thus, extrinsic effects

dominated the EIS response of µc-Li$_3$AlP$_2$ pellets. In Li-ion SEs, it is common that grain boundaries limit ion transport, although the underlying reason is unclear. Resistive Li-deficient secondary phases,[65] the creation of space charge layers in addition to the simple loss of the fast-ion transporting bulk crystal structure at the grain boundary[66] have all been postu-lated. Additionally, Symington et al.,[67] suggested that crystallo-graphic mismatch between differently-oriented grains can significantly impede ion transport between grains – this would be expected to be especially problematic when ion transport is strongly anisotropic as our simulations predict in Li$_3$AlP$_2$.

In contrast, nc-Li$_3$AlP$_2$ materials exhibited single semi-circles in the Nyquist plots with smaller impedances, which decreased with increasing x value and could be fit with one R-CPE unit (Fig. 9b). These results suggest a simplified and faster ionic conduction pathway compared to the microcrys-talline counterparts. These samples' σ_e values were low ($\approx 10^{-8}$ S cm^{-1}), with corresponding transference numbers >0.90 assuming all ion conduction was due to Li.

Time-dependent current decay experiments gave low values of σ_e (Fig. S6.1 in the ESI†). These measurements were used to
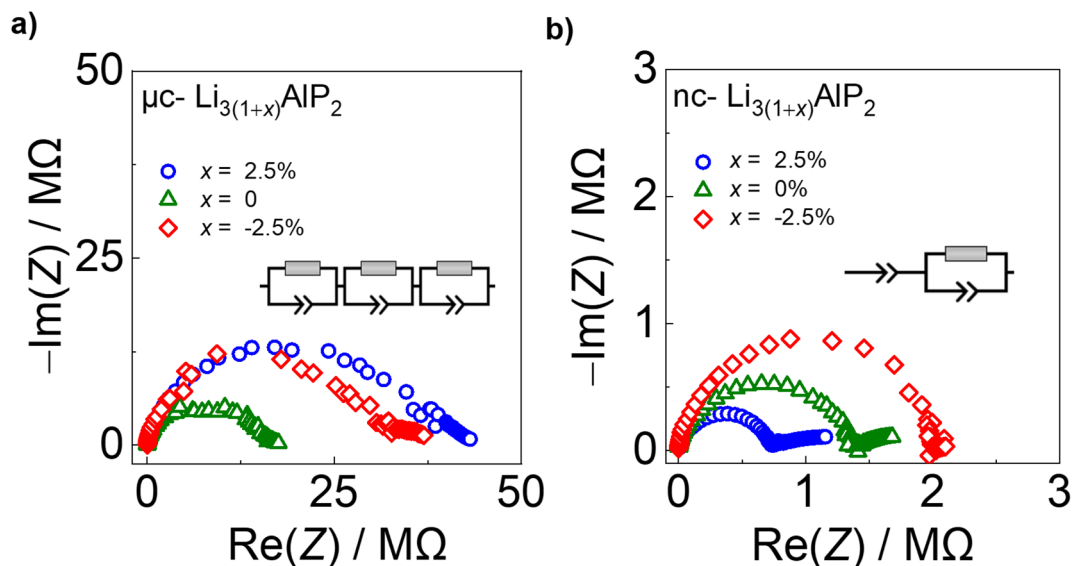
Fig. 9 Electrochemical impedance spectra for (a) μc-$Li_{3(1+x)}AlP_2$ and (b) nc-$Li_{3(1+x)}AlP_2$ with equivalent circuit models inset.

determine samples' ionic conductivity using eqn (3) (Fig. 10a). We first consider μc-$Li_{3(1+x)}AlP_2$, which had σ_{ion} values of $\approx 10^{-8}$ S cm^{-1} at room temperature. The comparable orders of magnitudes for σ_{ion} and σ_e resulted in low transference numbers ($=\sigma_{ion}/\sigma_{tot}$) assuming all ion conduction was due to Li.

These values of σ_{ion} (although too low for solid electrolyte applications) are appreciable, in contrast to the study of Restle et al., who found stoichiometric μc-Li_3AlP_2 to be an ionic insulator with capacitor-like behaviour observed using EIS.[16] This difference may be due to different annealing procedures: while we used evacuated fused silica ampules, Restle et al., used welded metal cans under an Ar atmosphere. Indeed, different synthetic results were obtained: those authors observed phase-

pure material after annealing at 700 °C, while at this temperature we observed impurity phases (Fig. 6a). We speculate that our annealing step under static vacuum facilitated greater loss of volatile elements during annealing, producing Li_3AlP_2 materials with higher concentrations of Li vacancies based on our computational analyses and thus, appreciable σ_{ion}. However, targeting samples with greater Li deficiency ($Li_{2.925}AlP_2$) or surplus ($Li_{3.025}AlP_2$) both resulted in a reduction in σ_{ion} by a factor of 2 (Fig. 10a), principally due to detrimental effects on grain boundary transport (Section S5 in the ESI†). We also note that σ_{ion} had no relationship to the Li_9AlP_4 impurity content from SXRD (Fig. 6b).
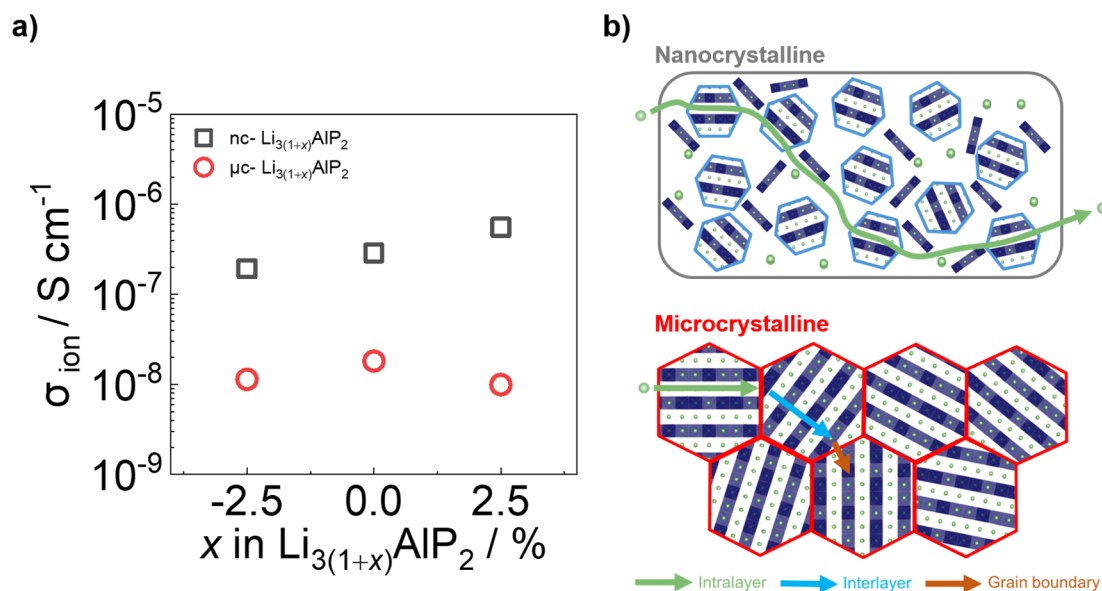

Fig. 10 (a) Ionic conductivities and (b) cartoon schematics for ion transport processes in nc-Li_3AlP_2 and μc-Li_3AlP_2 materials.

6436 | J. Mater. Chem. A, 2025, **13**, 6427–6439

This journal is © The Royal Society of Chemistry 2025

Approximately $10\times$ greater σ_{ion} values were observed for nc-Li_3AlP_2 materials, approaching 10^{-6} S cm^{-1} (Fig. 10a). Thus, both bulk and grain boundary resistances were greatly decreased in nanocrystalline form, where the long-range crystal structure is disrupted and grain boundaries removed (Fig. 10b). We note that the ionic conductivities for nc-Li_3AlP_2 are comparable to initial reports for Li agyrodites,[68] which, using site disorder strategies among others,[69] have since achieved $\sigma_{ion} \approx 10^{-2}$ S cm^{-1} at room temperature. The reason for the positive trend of σ_{ion} with nominal Li content, x in Fig. 10a is not entirely clear. It is uncorrelated with the amount of amorphous minor component present in the MAS NMR spectra (Section S3 in the ESI†), but is positively correlated with the intensities of low angle diffraction peaks (Fig. 6b): (020) and (200), corresponding to spacings between layers (Fig. 1c). This observation hints that some degree of layer integrity is beneficial to overall σ_{ion} and a complex relationship between intermediate-range order and ion transport in Li_3AlP_2.

4 Conclusions

In summary, we performed a computational and experimental investigation of ion transport in Li_3AlP_2. Defect calculations indicated that lithium ion transport via vacancies was more favorable than an interstitialcy mechanism. Hopping between Li sites was shown to have a relatively low energy barrier however, low native defect concentrations and anisotropy were also observed in simulations.

$Li_{3(1+x)}AlP_2$ ($x = -2.5, 0, 2.5\%$) powders were produced via ball milling of the elements followed by thermal annealing treatments. In several cases, minor impurity phases could only be detected using SXRD and solid-state NMR spectroscopy, highlighting the need for detailed characterisation of these materials. Microcrystalline, orthorhombic Li_3AlP_2 was achieved after heat treatment at 500 °C and facile Li$^+$ hopping was confirmed by dynamic NMR experiments ($E_a \approx 0.25$ eV). However, cold-pressed pellets exhibited low σ_{ion} values ($\approx 10^{-8}$ S cm^{-1}), and EIS analyses were consistent with slow transport in the bulk and at grain boundaries. Both may be a result of the strongly anisotropic ion migration pathways in the crystal structure.

Improved ionic conductivities were realised for nanocrystalline $Li_{3(1+x)}AlP_2$ samples produced by annealing at only 300 °C. Broader features in NMR spectroscopy and X-ray diffraction were seen, suggesting a disordered, nanocrystalline Li_3AlP_2 phase. PDF analysis revealed similar local motifs between the microcrystalline and nanocrystalline materials, with a domain size of ≈ 20 nm estimated in the latter. σ_{ion} values in the range 10^{-7} to 10^{-6} S cm^{-1} were determined on pellets by EIS that increased with x, while σ_e remained low. EIS spectra could be fit with a single relaxation feature, suggesting weaker bulk anisotropy and grain boundary effects as a result of structural disorder.

To conclude, both defect and disorder engineering was shown to positively affect ion transport in the Li_3AlP_2 system. Aliovalent doping to produce a greater number of vacancies (e.g., substitution of M^{4+} ions on the Al^{3+} site) and tuning of structural disorder via optimisation of synthetic conditions would be interesting avenues for future study. Additionally, there are limited studies on the electrochemical stability windows of phosphide-based solid electrolytes,[70] and further work in this area would be of great value. Our work should motivate the study of other compounds with anisotropic crystal structures, even those whose stoichiometric crystalline phases that do not exhibit desirable electrochemical properties in the solid-state.

Data availability

Synchrotron-based X-ray scattering data are available through repositories at ESRF (https://doi.esrf.fr/10.15151/ESRF-ES-953231276) and Diamond Light source (CY35411). Experimental (EIS and Lab based XRD, NMR) and computational calculation datasets to support the finding of this article are available from the Zenodo repository (https://doi.org/10.5281/zenodo.14714635).

Conflicts of interest

The authors declare no conflict of interest.

Acknowledgements

This journal is © The Royal Society of Chemistry 2025

J. Mater. Chem. A, 2025, 13, 6427–6439 | 6437

Notes and references

1 J. Janek and W. G. Zeier, *Nat. Energy*, 2023, **8**, 230–240.

2 T. Famprikis, P. Canepa, J. A. Dawson, M. S. Islam and C. Masquelier, *Nat. Mater.*, 2019, **18**, 1278–1291.

3 N. Kamaya, K. Homma, Y. Yamakawa, M. Hirayama, R. Kanno, M. Yonemura, T. Kamiyama, Y. Kato, S. Hama, K. Kawamoto and A. Mitsui, *Nat. Mater.*, 2011, **10**, 682–686.

4 Y. Kato, S. Hori, T. Saito, K. Suzuki, M. Hirayama, A. Mitsui, M. Yonemura, H. Iba and R. Kanno, *Nat. Energy*, 2016, **1**, 1–7.

5 T. Asano, A. Sakai, S. Ouchi, M. Sakaida, A. Miyazaki and S. Hasegawa, *Adv. Mater.*, 2018, **30**, 1803075.

6 S. Strangmüller, H. Eickhoff, D. Müller, W. Klein, G. Raudaschl-Sieber, H. Kirchhain, C. Sedlmeier, V. Baran, A. Senyshyn, V. L. Deringer, L. V. Wüllen, H. A. Gasteiger and T. F. Fässler, *J. Am. Chem. Soc.*, 2019, **141**, 14200–14209.

7 T. M. Restle, C. Sedlmeier, H. Kirchhain, W. Klein, G. Raudaschl-Sieber, V. L. Deringer, L. van Wüllen, H. A. Gasteiger and T. F. Fässler, *Angew. Chem., Int. Ed.*, 2020, **59**, 5665–5674.

8 E. Zintl and G. Brauer, *Z. Phys. Chem. B*, 1933, **20**, 245–271.

9 E. Zintl and W. Dullenkopf, *Z. Phys. Chem. B*, 1932, **16**, 183–194.

10 R. Nesper, *Prog. Solid State Chem.*, 1990, **20**, 1–45.

11 Y. Wang, W. D. Richards, S. P. Ong, L. J. Miara, J. C. Kim, Y. Mo and G. Ceder, *Nat. Mater.*, 2015, **14**, 1026–1031.

12 J. C. Bachman, S. Muy, A. Grimaud, H. H. Chang, N. Pour, S. F. Lux, O. Paschos, F. Maglia, S. Lupart, P. Lamp, L. Giordano and Y. Shao-Horn, *Chem. Rev.*, 2016, **116**, 140–162.

13 H. Eickhoff, S. Strangmüller, W. Klein, H. Kirchhain, C. Dietrich, W. G. Zeier, L. V. Wüllen and T. F. Fässler, *Chem. Mater.*, 2018, **30**, 6440–6448.

14 S. Strangmüller, D. Müller, G. Raudaschl-Sieber, H. Kirchhain, L. van Wüllen and T. F. Fässler, *Chem.–Eur. J.*, 2022, **28**, e20210421.

15 Z. Min, C. Yang, G. H. Zhong and Z. Lu, *ACS Appl. Mater. Interfaces*, 2022, **14**, 18373–18382.

16 T. M. Restle, J. V. Dums, G. Raudaschl-Sieber and T. F. Fässler, *Chem.–Eur. J.*, 2020, **26**, 6812–6819.

17 J. B. Goodenough, *Solid State Ionics*, 1997, **94**, 17–25.

18 A. G. Squires, D. O. Scanlon and B. J. Morgan, *Chem. Mater.*, 2020, **32**, 1876–1886.

19 R. Schlem, T. Bernges, C. Li, M. A. Kraft, N. Minafra and W. G. Zeier, *ACS Appl. Energy Mater.*, 2020, **3**, 3684–3691.

20 A. Jodlbauer, J. Spychala, K. Hogrefe, B. Gadermaier and H. M. R. Wilkening, *Chem. Mater.*, 2024, **36**, 1648–1664.

21 M. Brinek, C. Hiebl and H. M. R. Wilkening, *Chem. Mater.*, 2020, **32**, 4754–4766.

22 R. Schlem, C. F. Burmeister, P. Michalowski, S. Ohno, G. F. Dewald, A. Kwade and W. G. Zeier, *Adv. Energy Mater.*, 2021, **11**, 2101022.

23 H. Tan, L. Sun, Y. Zhang, K. Wang and Y. Zhang, *Adv. Sustain. Syst.*, 2022, **6**, 2200183.

24 W. Li, Y. Li, J.-H. Wang, S. Huang, A. Chen, L. Yang, J. Chen, L. He, W. K. Pang, L. Thomsen, *et al.*, *Energy Environ. Sci.*, 2024, **17**, 5387–5398.

25 G. Kresse and J. Hafner, *Phys. Rev. B:Condens. Matter Mater. Phys.*, 1993, **47**, 558–561.

26 G. Kresse and J. Furthmüller, *Comput. Mater. Sci.*, 1996, **6**, 15–50.

27 G. Kresse and J. Furthmüller, *Phys. Rev. B:Condens. Matter Mater. Phys.*, 1996, **54**, 11169–11186.

28 G. Kresse and D. Joubert, *Phys. Rev. B:Condens. Matter Mater. Phys.*, 1999, **59**, 1758–1775.

29 J. P. Perdew, A. Ruzsinszky, G. I. Csonka, O. A. Vydrov, G. E. Scuseria, L. A. Constantin, X. Zhou and K. Burke, *Phys. Rev. Lett.*, 2008, **100**, 136406.

30 J. Heyd, G. E. Scuseria and M. Ernzerhof, *J. Chem. Phys.*, 2003, **118**, 8207–8215.

31 A. V. Krukau, O. A. Vydrov, A. F. Izmaylov and G. E. Scuseria, *J. Chem. Phys.*, 2006, **125**, 224106.

32 A. R. McCluskey, S. W. Coles and B. J. Morgan, *J. Chem. Theory Comput.*, 2025, **21**(1), 79–87.

33 A. R. McCluskey, A. G. Squires, J. Dunn, S. W. Coles and B. J. Morgan, *J. Open Source Softw.*, 2024, **9**, 5984.

34 J. Buckeridge, D. Scanlon, A. Walsh and C. Catlow, *Comput. Phys. Commun.*, 2014, **185**, 330–338.

35 A. G. Squires, D. O. Scanlon and B. J. Morgan, *J. Open Source Softw.*, 2023, **8**, 4962.

36 S. R. Kavanagh, A. G. Squires, A. Nicolson, I. Mosquera-Lois, A. M. Ganose, B. Zhu, K. Brlec, A. Walsh and D. O. Scanlon, *J. Open Source Softw.*, 2024, **9**, 6433.

37 I. Mosquera-Lois, S. R. Kavanagh, A. Walsh and D. O. Scanlon, *npj Comput. Mater.*, 2023, **9**, 25.

38 P. Virtanen, R. Gommers, T. E. Oliphant, M. Haberland, T. Reddy, D. Cournapeau, E. Burovski, P. Peterson, W. Weckesser, J. Bright, S. J. van der Walt, M. Brett, J. Wilson, K. J. Millman, N. Mayorov, A. R. J. Nelson, E. Jones, R. Kern, E. Larson, C. J. Carey, İ. Polat, Y. Feng, E. W. Moore, J. VanderPlas, D. Laxalde, J. Perktold, R. Cimrman, I. Henriksen, E. A. Quintero, C. R. Harris, A. M. Archibald, A. H. Ribeiro, F. Pedregosa, P. van Mulbregt and SciPy 1.0 Contributors, *Nat. Methods*, 2020, **17**, 261–272.

39 C. R. Harris, K. J. Millman, S. J. Van Der Walt, R. Gommers, P. Virtanen, D. Cournapeau, E. Wieser, J. Taylor, S. Berg, N. J. Smith, *et al.*, *Nature*, 2020, **585**, 357–362.

40 W. McKinney, *Proceedings of the 9th Python in Science Conference*, 2010, pp. 56–61.

41 A. H. Larsen, J. J. Mortensen, J. Blomqvist, I. E. Castelli, R. Christensen, M. Dułak, J. Friis, M. N. Groves, B. Hammer, C. Hargus, E. D. Hermes, P. C. Jennings, P. B. Jensen, J. Kermode, J. R. Kitchin, E. L. Kolsbjerg, J. Kubal, K. Kaasbjerg, S. Lysgaard, J. B. Maronsson, T. Maxson, T. Olsen, L. Pastewka, A. Peterson, C. Rostgaard, J. Schiøtz, O. Schütt, M. Strange, K. S. Thygesen, T. Vegge, L. Vilhelmsen, M. Walter, Z. Zeng and K. W. Jacobsen, *J. Phys.: Condens. Matter*, 2017, **29**, 273002.

6438 | *J. Mater. Chem. A*, 2025, **13**, 6427–6439

This journal is © The Royal Society of Chemistry 2025

42 S. P. Ong, W. D. Richards, A. Jain, G. Hautier, M. Kocher, S. Cholia, D. Gunter, V. L. Chevrier, K. A. Persson and G. Ceder, *Comput. Mater. Sci.*, 2013, **68**, 314–319.

43 A. M Ganose, A. J Jackson and D. O Scanlon, *J. Open Source Softw.*, 2018, **3**, 717.

44 A. Togo, L. Chaput, T. Tadano and I. Tanaka, *J. Phys. Condens. Matter*, 2023, **35**, 353001.

45 A. Togo, *J. Phys. Soc. Jpn.*, 2023, **92**, 012001.

46 G. B. M. Vaughan, R. Baker, R. Barret, J. Bonnefoy, T. Buslaps, S. Checchia, D. Duran, F. Fihman, P. Got, J. Kieffer, S. A. J. Kimber, K. Martel, C. Morawe, D. Mottin, E. Papillon, S. Petitdemange, A. Vamvakeros, J.-P. Vieux and M. Di Michiel, *J. Synchrotron Radiat.*, 2020, **27**, 515–528.

47 K. Momma and F. Izumi, *J. Appl. Crystallogr.*, 2011, **44**, 1272–1276.

48 J. Kieffer and D. Karkoulis, *J. Phys.: Conf. Ser.*, 2013, 202012.

49 P. Juhás, T. Davis, C. L. Farrow and S. J. L. Billinge, *J. Appl. Crystallogr.*, 2013, **46**, 560–566.

50 C. L. Farrow, P. Juhas, J. W. Liu, D. Bryndin, E. S. Božin, J. Bloch, T. Proffen and S. J. L. Billinge, *J. Phys. Condens. Matter*, 2007, **19**(7), 335219.

51 S. Randau, D. A. Weber, O. Kötz, R. Koerver, P. Braun, A. Weber, E. Ivers-Tiffée, T. Adermann, J. Kulisch, W. G. Zeier, F. H. Richter and J. Janek, *Nat. Energy*, 2020, **5**, 259–270.

52 P. Vadhva, J. Hu, M. J. Johnson, R. Stocker, M. Braglia, D. J. L. Brett and A. J. E. Rettie, *ChemElectroChem*, 2021, **8**, 1930–1947.

53 T. H. Wan, M. Saccoccio, C. Chen and F. Ciucci, *Electrochim. Acta*, 2015, **184**, 483–499.

54 R. Juza and W. Schulz, *Z. Anorg. Allg. Chem.*, 1952, **269**, 1–12.

55 M. Dadsetani and S. Namjoo, *J. Mod. Phys.*, 2011, **2**, 929–933.

56 K. Kuriyama, J. Anzawa and K. Kushida, *J. Cryst. Growth*, 2008, **310**, 2298–2300.

57 S. Zhang and J. Northrup, *Phys. Rev. Lett.*, 1991, **67**, 2339–2342.

58 P. Scherrer, *Nachrichten von der Gesellschaft der Wissenschaften zu Göttingen, Mathematisch-Physikalische Klasse*, 1918, **1918**, 98–100.

59 U. Holzwarth and N. Gibson, *Nat. Nanotechnol.*, 2011, **6**, 534.

60 A. S. Masadeh, E. S. Božin, C. L. Farrow, G. Paglia, P. Juhas, S. J. L. Billinge, A. Karkamkar and M. G. Kanatzidis, *Phys. Rev. B:Condens. Matter Mater. Phys.*, 2007, **76**, 115413.

61 T. Zhao, A. N. Sobolev, X. Martinez de Irujo Labalde, M. A. Kraft and W. G. Zeier, *J. Mater. Chem. A*, 2024, **12**, 7015–7024.

62 O. H. Han, H. K. C. Timken and E. Oldfield, *J. Chem. Phys.*, 1998, **89**, 6046.

63 B. B. Duff, S. J. Elliott, J. Gamon, L. M. Daniels, M. J. Rosseinsky and F. Blanc, *Chem. Mater.*, 2023, **35**, 27–40.

64 J. T. S. Irvine, D. C. Sinclair and A. R. West, *Adv. Mater.*, 1990, **2**, 132–138.

65 C. Ma, K. Chen, C. Liang, C.-W. Nan, R. Ishikawa, K. More and M. Chi, *Energy Environ. Sci.*, 2014, **7**, 1638–1642.

66 A. R. Genreith-Schriever, J. P. Parras, H. J. Heelweg and R. A. De Souza, *ChemElectroChem*, 2020, **7**, 4718–4723.

67 A. R. Symington, M. Molinari, J. A. Dawson, J. M. Statham, J. Purton, P. Canepa and S. C. Parker, *J. Mater. Chem. A*, 2021, **9**, 6487–6498.

68 H.-J. Deiseroth, J. Maier, K. Weichert, V. Nickel, S.-T. Kong and C. Reiner, *Z. Anorg. Allg. Chem.*, 2011, **637**, 1287–1294.

69 L. Zhou, N. Minafra, W. G. Zeier and L. F. Nazar, *Accounts Chem. Res.*, 2021, **54**, 2717–2728.

70 Z. Min, C. Yang, G.-H. Zhong and Z. Lu, *ACS Appl. Mater. Interfaces*, 2022, **14**, 18373–18382.

This journal is © The Royal Society of Chemistry 2025

J. Mater. Chem. A, 2025, **13**, 6427–6439 | **6439**